International Journal of Heat and Fluid Flow 30 (2009) 778–788

Contents lists available at ScienceDirect

International Journal of Heat and Fluid Flow

journal homepage: www.elsevier.com/locate/ijhff

Effects of bubble size on heat transfer enhancement by sub-millimeter bubbles for laminar natural convection along a vertical plate

Atsuhide Kitagawa *, Kenji Uchida, Yoshimichi Hagiwara

Department of Mechanical and System Engineering, Kyoto Institute of Technology, Goshokaido-cho, Matsugasaki, Sakyo-ku, Kyoto 606-8585, Japan

ARTICLE INFO

Article history:
Received 30 June 2008
Received in revised form 19 December 2008
Accepted 9 February 2009
Available online 26 March 2009

Keywords:
Heat transfer enhancement
Bubble
Natural convection
Particle tracking velocimetry

ABSTRACT

Injection of sub-millimeter bubbles is considered a promising technique for enhancing natural convection heat transfer for liquids. So far, we have experimentally investigated heat transfer characteristics of laminar natural convection flows with sub-millimeter bubbles. However, the effects of the bubble size on the heat transfer have not yet been understood. The purpose of this study is to clarify the effects of the bubble size on the heat transfer enhancement for the laminar natural convection of water along a vertical heated plate with uniform heat flux. Temperature and velocity measurements, in which thermocouples and a particle tracking velocimetry technique are, respectively used, are conducted to investigate heat transfer and flow characteristics for different bubble sizes. Moreover, two-dimensional numerical simulations are performed to comprehensively understand the effects of bubble injection on the flow near the heated plate. The result shows that the ratio of the heat transfer coefficient with sub-millimeter-bubble injection to that without injection ranges from 1.3 to 2.2. The result also shows that for a constant bubble flow rate, the heat transfer coefficient ratio increases with a decrease in the mean bubble diameter. It is expected from our estimation based on both experimental data and simulation results that this increase results from an increase in the advection effect due to bubbles.

1. Introduction

Natural convection along a heated plate requires no driven devices such as pumps and fans, and thus the use of natural convection heat transfer provides cost savings and allows a high level of safety in heat exchanger systems. In the case of liquids, the natural convection heat transfer is seen in a wide variety of heat exchangers (e.g., electrical water heaters and solar water heaters) and cooling systems of small reactors. Details of the heat transfer characteristics for natural convections of liquids, particularly water, can be found in Vliet (1969), Lloyd et al. (1972), Shaukatullah and Gebhart (1978) and Inagaki and Komori (1995).

The use of dispersions (e.g., bubbles and particles) has been considered a promising technique for enhancing natural convection heat transfer. Tamari and Nishikawa (1976) and Tokuhiro and Lykoudis (1994a,b) investigated experimentally the effects of gas-bubble injection on natural convection heat transfer along a heated vertical plate in a liquid. Each research group showed the heat transfer coefficient is significantly increased by mixing due to gas-bubbles. However, the gas-bubble injection technique, in which a few-millimeter bubbles were used, required large amounts of gas to increase the bubble number density in the vicinity of the heated vertical plate (e.g., a gas flow rate of 900–9200 mm^3/s was used in the study of Tokuhiro and Lykoudis (1994a)). The increase in the energy for injecting gas-bubbles into a flow results in a decrease in the heat transfer gain. In contrast, we focused on the relationship between the bubble size and the thermal boundary layer thickness and used sub-millimeter bubbles to enhance the heat transfer for laminar natural convection along a heated vertical plate. Consequently, it was found that at bubble flow rates lower than 60 mm^3/s, the heat transfer coefficient with sub-millimeter-bubble injection is up to 2.0 times that without injection (Kitagawa et al. 2008). It was also found that the ratio of the heat transfer rate obtained with the sub-millimeter-bubble injection to the power consumption of the sub-millimeter-bubble generation was 3.5–5.5. These results clearly demonstrate that sub-millimeter-bubble injection is a highly efficient technique for enhancing natural convection heat transfer. Moreover, the simultaneous measurement of temperature and velocity showed that the heat transfer enhancement is deeply related to flow and temperature modifications induced by bubble motions near the heated plate (Kitagawa et al. 2008). From this result, we expect the heat transfer gain depends strongly on bubble size. Therefore, we need information on temperature and velocity measurements for different bubble sizes to obtain optimum conditions for natural convection heat transfer enhancement.

The purpose of this study is to clarify the effects of the bubble size on the heat transfer enhancement for laminar natural convection of water along a vertical heated plate. Temperature

* Corresponding author. Tel.: +81 75 724 7324; fax: +81 75 724 7300.
E-mail address: kitagawa@kit.ac.jp (A. Kitagawa).

0142-727X/$ - see front matter © 2009 Elsevier Inc. All rights reserved.
doi:10.1016/j.ijheatfluidflow.2009.02.008

Nomenclature

A_H	surface area of heated plate
A_{st}	overall surface area of stainless-steel foil
d	bubble equivalent diameter
d_m	mean bubble diameter
F	Faraday constant
F_A	ideal driving force
FC_A, FC_M, FC_H	advection, mixing and heat insulation effects due to bubbles
FC_0	net increase in heat transfer coefficient due to bubble injection
g	gravitational acceleration
h_x	heat transfer coefficient with bubble injection
h_{x0}	heat transfer coefficient without bubble injection
h_{xA}	heat transfer coefficient obtained from numerical simulations of natural convection with F_A
I	electrical current
$\mathbf{i}_x$	unit vector in x direction
k	thermal conductivity
L_x, L_y	lengths of computational domain in x and y directions
l	total length of stainless-steel foil
n	number of bubbles
N	sum of all n
Nu_x	local Nusselt number
P	power consumption of bubble generation
p	pressure
Q	bubble flow rate
$\dot{Q}_e$	heat transfer rate obtained with bubble injection
q_w	wall heat flux
R_0	universal gas constant
Ra_x^*	modified Rayleigh number
Re_d	bubble Reynolds number
S	cross-section area of stainless-steel foil
T	temperature
$\mathbf{u}$	velocity vector
u	mean velocity in x direction
$u_{L,max}$	maximum liquid rise velocity
v	mean velocity in y direction
x, y, z	streamwise, wall-normal and spanwise directions
y_p	y location of peak in liquid rise velocity profile

Greek symbols

α	thermal diffusivity
β	coefficient of volume expansion
Δx, Δy	grid intervals in x and y directions
η	heat transfer gain
ν	kinematic viscosity
θ	angle between stainless-steel plate and top plate of bubble generator
ρ	density
ρ'	specific electrical resistance of stainless-steel foil

Subscripts

G	gas
L	liquid
w	wall condition
∞	ambient condition

measurements using thermocouples and velocity measurements using a particle tracking velocimetry (PTV) technique are conducted to investigate heat transfer and flow characteristics for different bubble sizes. Two-dimensional numerical simulations are also conducted to examine the validity of experimental data and to comprehensively understand the effects of bubble injection on the flow near the heated plate. Tap water is used for working fluid and hydrogen bubbles generated by electrolysis are used as the sub-millimeter bubbles.

2. Experimental setup

2.1. Experimental apparatus

A schematic diagram of the experimental apparatus is shown in Fig. 1. This apparatus consists of a container made of 10 mm thick transparent acrylic resin plates (1200 mm height, 140 mm width, 150 mm depth), a bubble generator, a vertical plate with uniform heat flux, a DC power supply (Takasago, EX-375H), a cooling plate (Sensor Controls, CHP-77HI) and a temperature controller (Yamatake, FC-2410). The bubble generator is set at the bottom of the container. The vertical plate with uniform heat flux, which is called the "heated plate" in the following, is attached to the inner sidewall of the container. The temperature of the ambient liquid is controlled using the cooling plate and temperature controller.

The container is filled with water of 20 °C to 50 mm from the top and the water is thoroughly mixed. It is then left for at least 10 min to reduce liquid disturbance. As an electrolyte for bubble generation, a small amount of salt is injected into the water. The salt concentration is approximately 0.3%, and it is therefore considered that the physical properties of the liquid are the same as those of water. The x, y and z axes are, respectively, set along the streamwise, wall-normal and spanwise directions. $x = 0$, $y = 0$ and $z = 0$ are set at the starting point of the heating section, at the surface of the heated plate and at the center of the container in the spanwise direction, respectively.

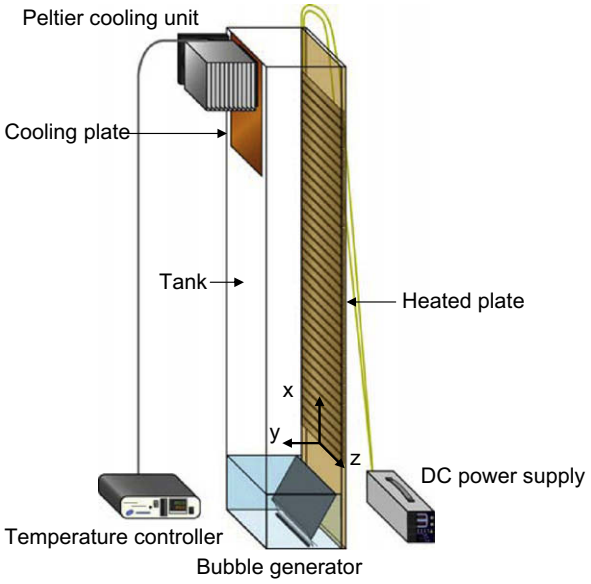

Fig. 1. Schematic diagram of the experimental apparatus.

2.2. Bubble generator

Sub-millimeter bubbles used in this study are generated by electrolysis. This generation method is the same as that in our previous study and the advantages of this method can be seen in Kitagawa et al. (2008). The bubble flow rate Q is defined as

$$Q = \frac{IR_0T_{L,\infty}}{2Fp}, \quad (1)$$

where I is the electrical current through the electrodes, R_0 is the universal gas constant ($R_0 = 8.31 \times 10^9$ Pa mm^3/(K mol)), $T_{L,\infty}$ is the temperature of the ambient liquid ($T_{L,\infty} = 293$ K), F is the Faraday constant ($F = 9.65 \times 10^4$ A s/mol) and p is the pressure ($p = 1.13 \times 10^5$ Pa).

As shown in Fig. 2, the bubble generator consists of 5-mm thick transparent acrylic resin plates, a 0.5-mm thick stainless-steel plate, a platinum wire (0.05 mm in diameter and 100 mm long) and a carbon rod (15 mm in diameter and 100 mm long) and a charcoal absorber. The platinum wire is used as the cathode. The carbon rod is applied as the anode instead of the platinum wire used in our previous study because of a reduction in the power consumption of the sub-millimeter-bubble generation. Both electrodes are set at the bottom of the bubble generator. There is the possibility that chlorine bubbles generated at the anode will corrode the surface of the heated plate, so a partition is set between the electrodes to prevent the chlorine bubbles from migrating toward the measurement region. The chlorine bubbles are completely removed using the charcoal absorber. The bubble exit width of the generator is approximately 2.0 mm. The generation of the bubbles is conducted from 390 to 480 s after the heating of the vertical plate starts.

2.3. Heated plate

A schematic diagram of the heated plate is shown in Fig. 3. The stainless-steel foils (165 mm long, 25 mm wide, 0.02 mm thick) are attached to acrylic resin plate 1 (1200 mm high, 149 mm wide, 10 mm thick) at 0.4 mm intervals to electrically heat the plate under uniform heat flux conditions. The specific electrical resistance of each foil ρ' is 7.4×10^{-7} Ω m. The foils are connected in series with copper wires and are heated using the DC power supply. Details of the heated plate are given in Kitagawa et al. (2008). The starting point of the heating section is located 50 mm above the top of the bubble generator. The heating of the vertical plate is performed in the region of $0 < x < 914$ mm.

2.4. Bubble diameter

In our experiments, the bubble diameter is controlled by changing the angle between the stainless-steel plate and the top plate of the bubble generator, θ, which is seen in Fig. 2. The angle is changed from 15 to 75° in 15° intervals. The location of the cathode is changed so that the distance between the stainless-steel plate and cathode is kept constant. Fig. 4 shows the probability distributions of the bubble equivalent diameter d for different angles. In this figure, n is the number of bubbles for each diameter, and N is the sum of all n. For all angles, the bubble diameters are smaller than 1 mm. Moreover, the bubble diameter becomes smaller with an increase in the angle and is almost independent of the bubble flow rate. In the following sections, the angle is set as $\theta = 15$, 45 and 75°, considering the above results. The mean bubble diameters d_m for $\theta = 15$, 45 and 75° are 0.70 ± 0.03, 0.51 ± 0.03 and 0.30 ± 0.02 mm, respectively. In the following, these diameters are described for convenience as 0.70, 0.51 and 0.30 mm.

When generating bubbles by electrolysis, it may happen that the heat generated at the electrodes causes errors in the temperature measurements. To investigate the heat generated at the electrodes, a preliminary experiment was conducted. The liquid temperature at the bubble exit of the bubble generator was measured using a temperature measurement system, which is explained in Section 3.1. Experimental data show the increase in

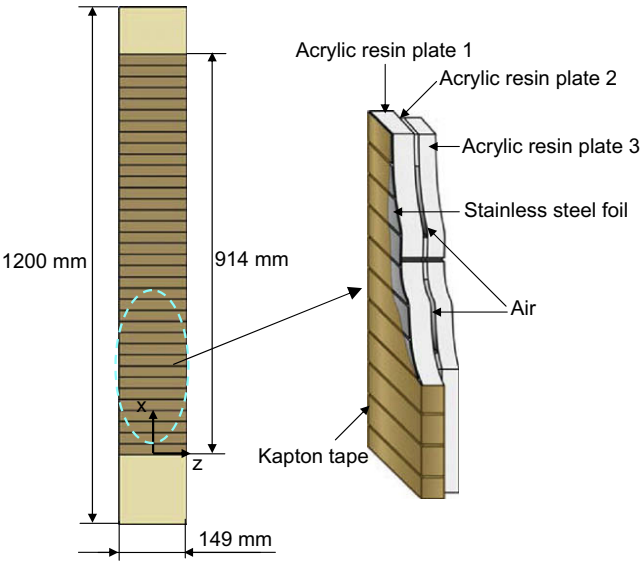

Fig. 3. Schematic diagram of the heated plate.

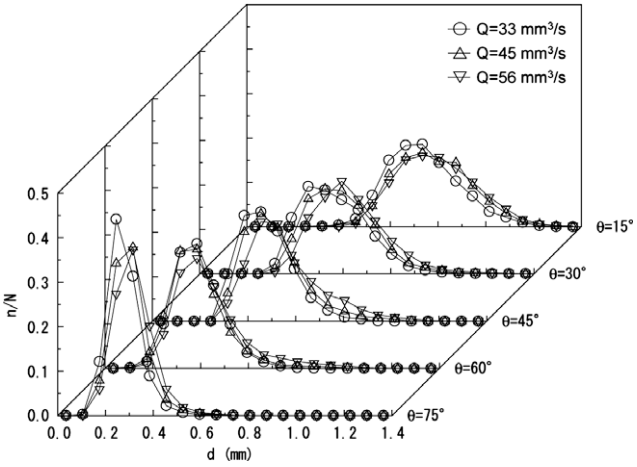

Fig. 4. Probability distributions of bubble equivalent diameter for different angles.

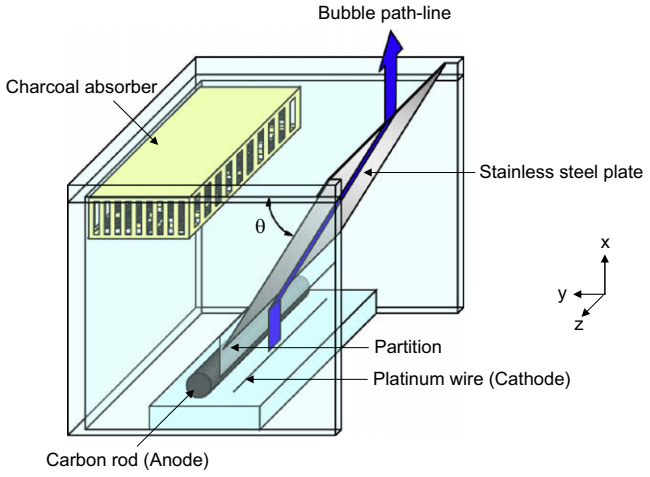

Fig. 2. Schematic diagram of the bubble generator.

Table 1
Experimental conditions.

Temperature measurement	
Temperature of ambient liquid	$T_{L,\infty}$ = 20.0 ± 0.1 °C
Bubble flow rate	Q = 33, 45, 56 mm^3/s
Wall heat flux	q_w = 533, 947, 1480 W/m^2
Mean bubble diameter	d_m = 0.30, 0.51, 0.70 mm
Measurement position	x = 70, 170, 270 mm, z = ±20 mm
Velocity measurement	
Temperature of ambient liquid	$T_{L,\infty}$ = 20.0 ± 0.1 °C
Bubble flow rate	Q = 33, 56 mm^3/s
Wall heat flux	q_w = 947 W/m^2
Mean bubble diameter	d_m = 0.30, 0.51, 0.70 mm
Measurement position	x = 170 mm, z = 20 mm

liquid temperature is less than 0.1 °C, and therefore the effect of the heat generated at the electrodes on the temperature field is considered negligible.

2.5. Experimental conditions

Table 1 shows the experimental conditions for each of the temperature and velocity measurements. In the velocity measurements, the wall heat flux q_w and measurement position x are respectively set as 947 W/m^2 and 170 mm to allow detailed discussion of flow modifications by bubbles of different diameters and flow rates. q_w is estimated from Eq. (2).

$$q_w = \frac{\rho' I l^2}{S A_{st}}, \tag{2}$$

where l, S and A_{st} are the total length, cross-sectional area and overall surface area of the stainless-steel foil, respectively. The dependency of the specific electrical resistance on temperature is ignored because in our experiments the wall temperature ranges from 20 to 25 °C.

3. Temperature measurement technique

3.1. Temperature measurement system

The temperature measurement system consists of K-type 100 μm thermocouples, a reference junction and a high-speed data acquisition unit (Yokogawa, MX100). The thermocouples, which are accurate within ±0.12 °C, are used to simultaneously measure the surface temperature of the heated plate T_w and the water temperature distant from the heated plate. The thermocouples for measuring T_w are set at x = 70, 170, 270 mm and z = ±20 mm. The high-speed data acquisition unit is directly connected to a personal computer monitor the thermoelectric force of the thermocouples in real time. A thermostatic bath is used for calibrating the thermocouple temperature readings. The sampling frequency for the temperature measurement is 5 Hz and the measurement period is 480 s.

3.2. Estimation of the local heat transfer coefficient

As described in Section 2.3, the vertical plate is heated under uniform heat flux conditions, so that the local heat transfer coefficient h_x at each of the measurement positions is obtained from Eq. (3).

$$h_x = \frac{q_w}{T_w - T_{L,\infty}}, \tag{3}$$

where the subscript L stands for the liquid. In our experiments, the total uncertainly in the heat transfer coefficient associated with both the thermocouple accuracy and the heat loss through the back of the heated plate is estimated to be approximately 6%.

4. Velocity measurement technique

4.1. Simultaneous velocity measurement technique

In this study, the PTV technique is applied to simultaneous two-phase velocity measurement and a shadow image technique is used for clearly obtaining the bubble interface. Details of these techniques are given in Kitagawa et al. (2005).

4.2. Velocity measurement system

A schematic diagram of the two-phase velocity measurement system is shown in Fig. 5. A digital color CCD camera (Imperx, VGA210-LC), which is set in front of the container, is used to capture the tracer particle and bubble images. Particles of 60 μm in mean diameter and 1.02 in specific gravity are used as the tracer particles and the particle concentration is approximately 100 ppm. Two halogen-light sources (Moritex, MHAB-150 W) are used for illuminating the tracer particle and bubble. One halogen-light source for the tracer particle is set at the side of the container. A light sheet with a thickness of 5 mm is produced with a line light guide, a cylindrical lens, a blue-pass filter and a slit. The other halogen-light source for the bubble is set behind the container. The light emitted from the halogen-light source passes through a red-pass filter and illuminates bubbles in the vicinity of the heated plate. Consequently, the bubble images are captured as shadow images. The measurement area is $163 < x < 177$ mm, $0 < y < 11$ mm and $17.5 < z < 22.5$ mm. Images of 600 × 480 pixels, which are taken with the color CCD camera, are directly recorded by a personal computer. The spatial resolution is 0.023 mm/pixel. The exposure time of the color CCD camera is 0.001 s and the frame rate is 110–130 fps depending on the different experimental conditions.

4.3. Measurement uncertainty

In the two-phase velocity measurement described above, liquid tracer particles are captured in the blue images and bubbles are captured in the red images. Separation of the two-phases is performed based on both blue and red images. The bubble diameter is calculated from the equivalent area of each bubble image. Details of the image processing technique for obtaining the two-phase velocities are given in Kitagawa et al. (2007). The uncertainty in the bubble velocity associated with the bubble centroid detection is estimated to be 0.49 mm/s, and therefore the error in this value relative to the maximum bubble rise velocity (126.5 mm/s) is 0.4%.

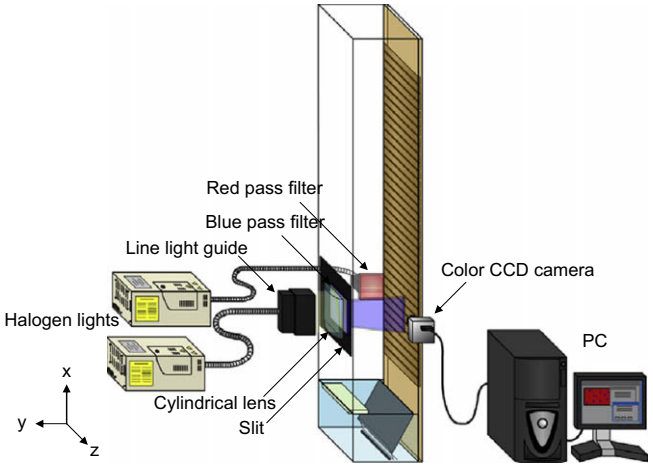

Fig. 5. Schematic diagram of the two-phase velocity measurement system.

On the other hand, the uncertainty in the liquid velocity associated with the particle centroid detection is estimated to be 0.55 mm/s. Hence, the error in this value relative to the maximum liquid rise velocity (33.4 mm/s) is 1.6%. To obtain highly accurate statistical data for both phases, which are presented in Section 6, we used more than 5500 images for each of the experimental conditions.

5. Numerical simulation method

5.1. Assumptions

The main assumptions in the numerical simulation are as follows:

(1) The flow is two-dimensional laminar flow.
(2) The density is constant in the governing equations mentioned in Section 5.3 except for that in the buoyancy term (Boussinesq approximation).

5.2. Computational domain

The configuration of the axes is the same as that described in Section 2.1. The lengths of the computational domain in the x and y directions are, respectively set as $L_x = 1037$ mm and $L_y = 120$ mm, considering both the sizes of the container and the bubble generator used in the experiments. Non-slip conditions are imposed for the bottom and both sidewalls of the computational domain. The heating region under uniform heat flux conditions is set as $x = 0$–914 mm and is the same as the region described in Section 2.3. On the other hand, a free-slip condition with a constant temperature ($T = 20$ °C) is imposed for the top of the computational domain to express the gas–liquid interface. The grid intervals in the x and y directions are $\Delta x = 1$ mm and $\Delta y = 0.5$ mm, respectively.

5.3. Governing equations

The governing equations are as follows:

(1) Conservation equation for the liquid mass:

$$\nabla \cdot \mathbf{u}_L = 0, \tag{4}$$

where $\mathbf{u}$ is the velocity vector.

(2) Conservation equation for the liquid momentum:

$$\frac{\partial \mathbf{u}_L}{\partial t} + (\mathbf{u}_L \cdot \nabla)\mathbf{u}_L = -\frac{1}{\rho_L}\nabla p_L + \nu_L \nabla^2 \mathbf{u}_L + (\beta_L(T_L - T_{L,\infty})g - g)\mathbf{i}_x, \tag{5}$$

where ρ is the density, β is the coefficient of volume expansion, g is the gravitational acceleration, ν is the kinematic viscosity and $\mathbf{i}_x$ is the unit vector in the x direction. The first term in the parentheses on the right-hand side is the buoyancy force induced by the density difference in the liquid.

(3) Conservation equation for the liquid energy:

$$\frac{\partial T_L}{\partial t} + (\mathbf{u}_L \cdot \nabla)T_L = \alpha_L \nabla^2 T_L, \tag{6}$$

where α is the thermal diffusivity.

The governing equations are discretized by the finite differential method and all the spatial derivative terms in Eqs. (4)–(6) are discretized with a staggered grid system. A simplified marker-and-cell (SMAC) method is used for pressure–velocity coupling. A two-dimensional cubic-interpolated propagation (CIP) scheme, which was proposed by Takewaki and Yabe (1987), is applied to the advection terms in Eqs. (5) and (6). The viscous term in Eq. (5) and the thermal conductivity term in Eq. (6) are discretized in space by the second-order central difference scheme.

6. Results and discussion

6.1. Validity of experimental data and simulation results without bubble injection

In this section, we examine the validity of experimental data and simulation results without bubble injection. The relationship between the modified Rayleigh number Ra_x^* and the local Nusselt number Nu_x is shown in Fig. 6. The dimensionless parameters are defined as

$$Ra_x^* = \frac{\beta q_w x^4 g}{k\nu\alpha}, \quad Nu_x = \frac{h_x x}{k}, \tag{7}$$

where k is the thermal conductivity. The physical properties in Eq. (7) are evaluated at the film temperature. For comparison, the following empirical equation for laminar natural convection along a vertical plate with uniform heat flux (Vliet and Liu, 1969) is added to the figure as a solid line.

$$Nu_x = 0.6 Ra_x^{*1/5}. \tag{8}$$

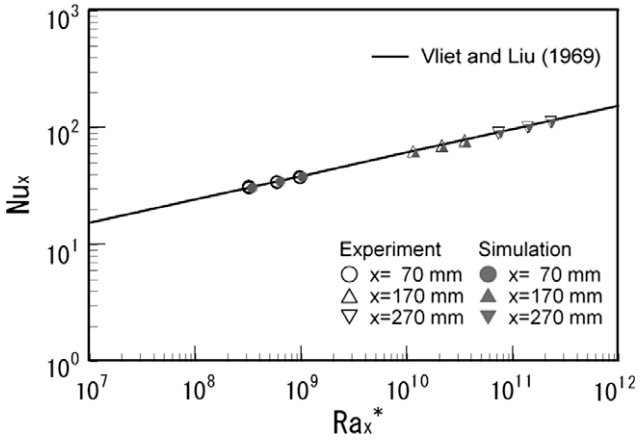

Fig. 6. Relationship between Ra_x^* and Nu_x without bubble injection.

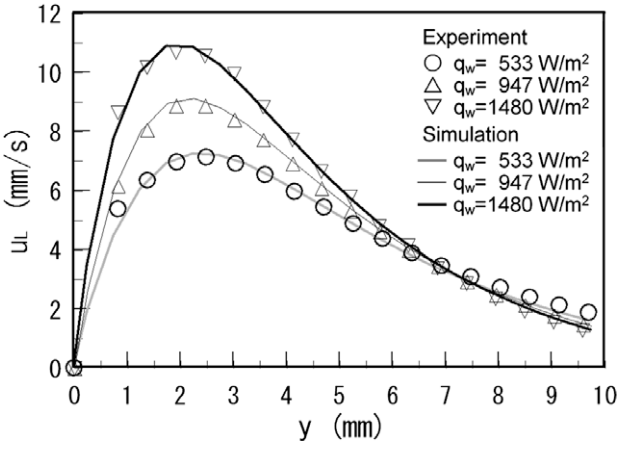

Fig. 7. Profiles of liquid rise velocity without bubble injection.

It is clear from Fig. 6 that the experimental data and the simulation results agree well with the empirical equation. The maximum difference between the two is 3.2% for the former and 3.6% for the latter. Hence, both the experimental data for the temperature measurements and the simulation results are valid for the laminar natural convection boundary layer of water along the vertical plate.

Next, the experimental data for velocity measurements are compared with simulation results. Fig. 7 shows the profiles of the liquid rise velocity. In this figure, u is the mean velocity in the x direction. It is seen from Fig. 7 that the experimental data are in agreement with the simulation results except for the velocity in the vicinity of the heated plate in the case of low wall heat flux. Therefore, the experimental data for the velocity measurements are also valid for the laminar natural convection boundary layer of water along the vertical plate.

6.2. Heat transfer characteristics with sub-millimeter-bubble injection

The heat transfer characteristics with sub-millimeter-bubble injection are shown in Fig. 8 (d_m vs h_x/h_{x0}), Fig. 9 (q_w vs h_x/h_{x0}) and Fig. 10 (x vs h_x/h_{x0}). In each figure, h_x and h_{x0} are, respectively, the heat transfer coefficients with and without sub-millimeter-bubble injection and the latter is estimated from Eq. (8). In the following, h_x/h_{x0} is called the "heat transfer coefficient ratio". The error bar in each of the figures represents a 95% confidence level in the experimental data. The following points are discussed for these figures.

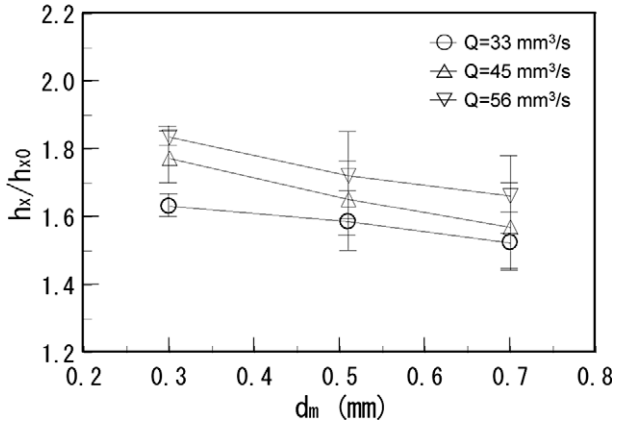

Fig. 8. Relationship between d_m and h_x/h_{x0} at $x = 170$ mm and $q_w = 947$ W/m^2.

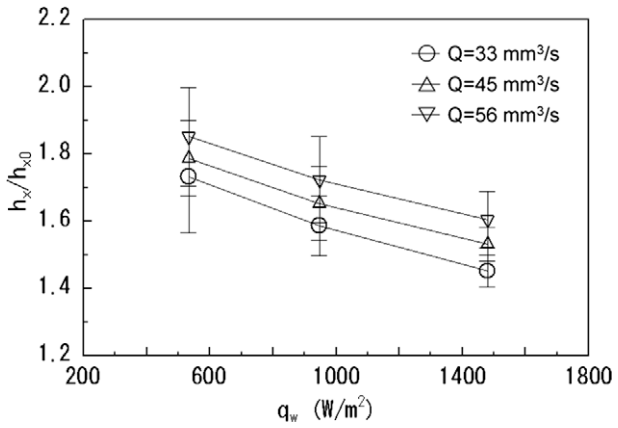

Fig. 9. Relationship between q_w and h_x/h_{x0} at $x = 170$ mm and $d_m = 0.51$ mm.

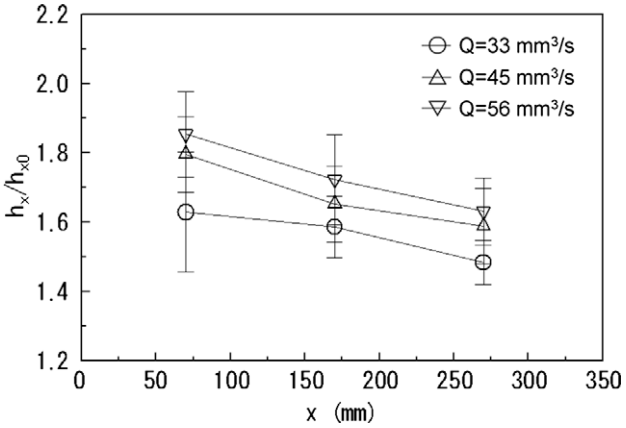

Fig. 10. Relationship between x and h_x/h_{x0} at $q_w = 947$ W/m^2 and $d_m = 0.51$ mm.

(1) The heat transfer coefficient ratios are much higher than 1.0 as a result of bubble injection (see Figs. 8–10). For all experimental conditions used in this study, the heat transfer ratio ranges from 1.3 to 2.2. This clearly demonstrates that the use of sub-millimeter bubbles with mean diameters in the range of $d_m = 0.33–0.71$ mm results in significant heat transfer enhancement for the laminar natural convection of water.

(2) The heat transfer coefficient ratios increase with a decrease in the mean bubble diameter (see Fig. 8). For instance, the heat transfer coefficient ratio is 1.6–1.8 for $d_m = 0.30$ mm and 1.5–1.7 for $d_m = 0.70$ mm. It is therefore possible to effectively enhance the natural convection heat transfer by bubble size reduction. Moreover, the heat transfer coefficient ratios increase with the bubble flow rate. The rate of increase in the heat transfer coefficient ratio between $Q = 33$ and 56 mm^3/s is 9–13% for all the mean bubble diameters.

(3) The heat transfer coefficient ratios decrease with an increase in the wall heat flux (see Fig. 9). The rate of decrease in the heat transfer coefficient ratio between $q_w = 533$ and 1480 W/m^2 is 13–16% for all the bubble flow rates. That is, at lower wall heat fluxes, sub-millimeter-bubble injection is more effective for heat transfer enhancement. This tendency is also seen in the case of other mean bubble diameters and the rate of decrease in the heat transfer coefficient ratio is 14–19%.

(4) The heat transfer coefficient ratios decrease with an increase of x (see Fig. 10). The rate of decrease in the heat transfer coefficient ratio between $x = 70$ and 270 mm is 9–12% for all the bubble flow rates. The same tendency is observed in the case of other mean bubble diameters.

6.3. Heat transfer gain

The relationship between the bubble flow rate and heat transfer gain η is shown in Fig. 11. The heat transfer gain is the ratio of the heat transfer rate obtained with the sub-millimeter-bubble injection $\dot{Q}_e$ to the power consumption of the sub-millimeter-bubble generation P and is defined as:

$$\eta = \frac{\dot{Q}_e}{P} = \frac{q_w A_H (h_x/h_{x0} - 1)}{P}, \tag{9}$$

where A_H is the surface area of the heated plate. For comparison, the data obtained from our previous measurements (Kitagawa et al., 2008) are added to the figure. It is noted that the surface area, measurement position and wall heat flux are the same as those in our

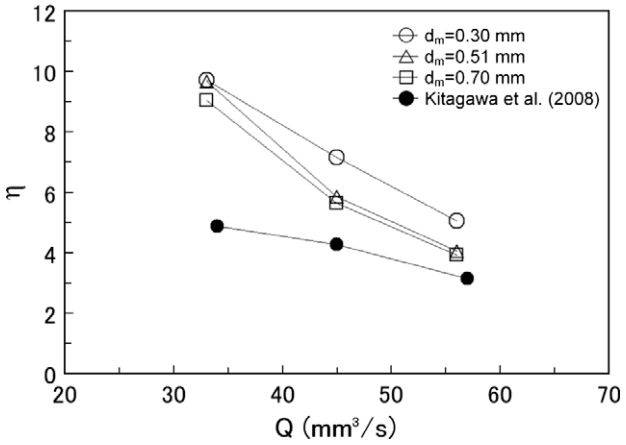

Fig. 11. Relationship between bubble flow rate and heat transfer gain.

previous study; i.e., $A_H = 600\ \text{mm} \times 149\ \text{mm}$, $x = 170\ \text{mm}$ and $q_w = 533\ \text{W/m}^2$. The heat transfer gains for the present measurements are higher than those for our previous measurements. This is due to the anode being changed from platinum wire of 0.1 mm diameter to a carbon rod of 15 mm diameter. In the present measurements, the heat transfer gain increases with a decrease in the mean bubble diameter, and it is therefore possible to effectively increase the heat transfer gain as well as the heat transfer coefficient ratio by bubble size reduction. Furthermore, the heat transfer gain reaches approximately 9.7. This clearly demonstrates that sub-millimeter-bubble injection is a highly efficient technique for enhancing the natural convection heat transfer of water along a vertical flat plate.

6.4. Instantaneous two-phase velocity field

Fig. 12 illustrates a typical instantaneous two-phase velocity field for the case of $d_m = 0.51$ mm and $Q = 56\ \text{mm}^3/\text{s}$. The right-hand side of the image corresponds to the surface of the heated plate. In this figure, the arrow represents the velocity vector, the black solid circle is a bubble located in the measurement plane, and the gray solid circle is a bubble located out of the measurement plane. The magnitude of the bubble velocity vectors is set as 1/10 of the actual magnitude. It is found from this figure that the liquid velocity vectors and the bubble velocity vectors are obtained completely independently.

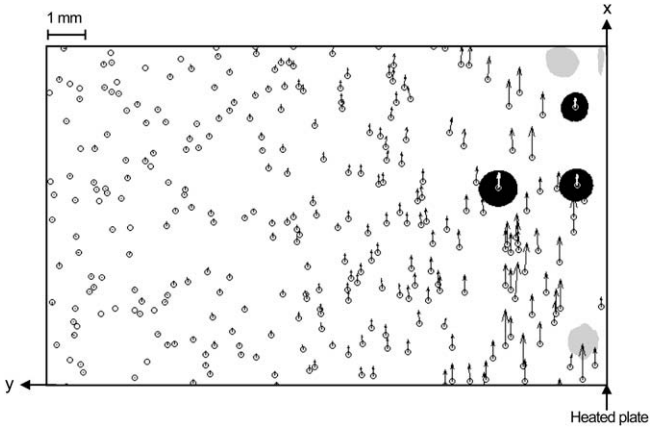

Fig. 12. Typical instantaneous two-phase velocity field for the case of $d_m = 0.51$ mm and $Q = 56\ \text{mm}^3/\text{s}$.

6.5. Bubble location

The probability distributions of the bubble location at $Q = 33\ \text{mm}^3/\text{s}$ are shown in Fig. 13. In this figure, n is the number of bubbles at each y location. For all the mean bubble diameters, bubbles are located in the region of $y = 0$–2.0 mm. Moreover, the locations of the peaks in the distributions for $d_m = 0.30$, 0.51 and 0.70 mm are, respectively, $y = 0.22$, 0.65 and 1.02 mm; i.e., smaller bubbles tend to concentrate near the heated plate. In particular, in the case of $d_m = 0.30$ mm, the distance between the peak location and the heated plate is short compared with the mean bubble diameter. It is therefore expected that the probability of the direct contact between bubbles and the heated plate is relatively high. In our experiments, the gas inside the bubble is hydrogen while the working fluid is water, and the thermal conductivity of the former is much lower than that of the latter. For this reason, it may happen that in the case of $d_m = 0.30$ mm, the bubble concentration near the heated plate leads to the "heat insulation effect", which causes heat transfer deterioration. On the other hand, in the cases of $d_m = 0.51$ and 0.70 mm, the distance is long compared with the mean bubble diameter. This means that the probability of the direct contact between bubbles and the heated plate is sufficiently low. Hence, the heat insulation effect is considered negligible for both cases.

6.6. Bubble mean velocity

Fig. 14 shows the profiles of the bubble mean velocities at $Q = 33\ \text{mm}^3/\text{s}$. The subscript G stands for the bubble and v is the mean velocity in the y direction. In this figure, it is noted that the results for more than 100 samples are presented. Over a wide range of y, the bubble rise velocity increases with an increase in the bubble diameter. This is because the buoyancy force acting on the bubbles increases with the bubble diameter, as expected. In contrast, according to our estimation using terminal velocity of each bubble, the ratio of the bubble rise velocity shown in Fig. 14 to the bubble terminal velocity for $d_m = 0.30$ mm is higher than that for $d_m = 0.70$ mm. This is related to the liquid rise velocity induced by bubbles and it is discussed in Section 6.7.

Next, we focus on the bubble Reynolds number Re_d, which is defined as

$$Re_d = \frac{|\mathbf{u}_G - \mathbf{u}_L| \cdot d}{\nu_L}. \tag{10}$$

It is estimated from our calculations that the bubble Reynolds number is 15–25 for $d_m = 0.30$ mm, 20–50 for $d_m = 0.51$ mm and 40–100 for $d_m = 0.70$ mm. For all the mean bubble diameters, the

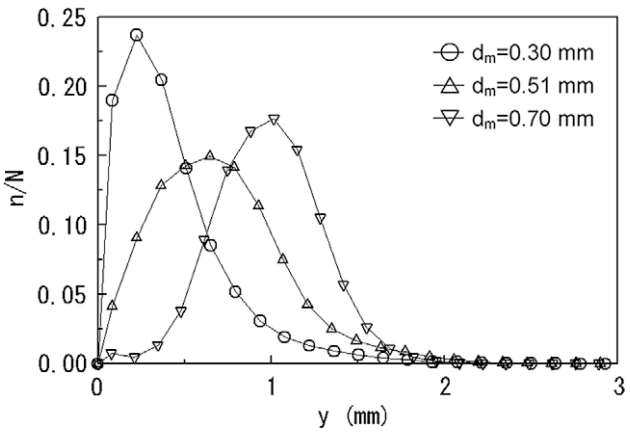

Fig. 13. Probability distributions of bubble location at $Q = 33\ \text{mm}^3/\text{s}$.

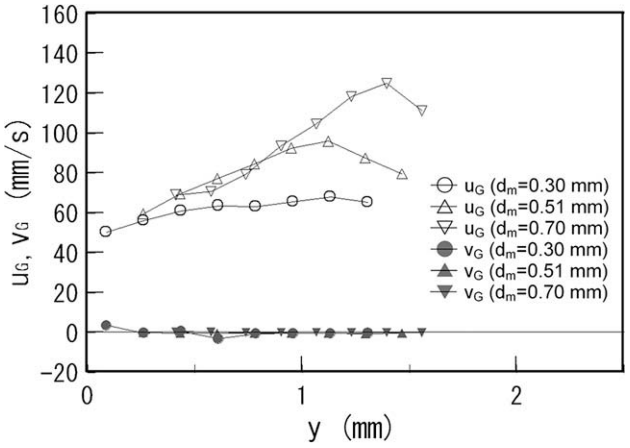

Fig. 14. Profiles of bubble mean velocities at $Q = 33$ mm^3/s.

bubble Reynolds numbers are lower than 100. Therefore, the deformation of and the vortex shedding from the bubble surface are ignored in our experiments.

6.7. Liquid velocity characteristics

Figs. 15 and 16 show the profiles of the liquid mean velocities and the liquid velocity fluctuation, $\langle u'_L u'_L + v'_L v'_L \rangle^{1/2}$, respectively. Case (a) is the result for a constant bubble flow rate

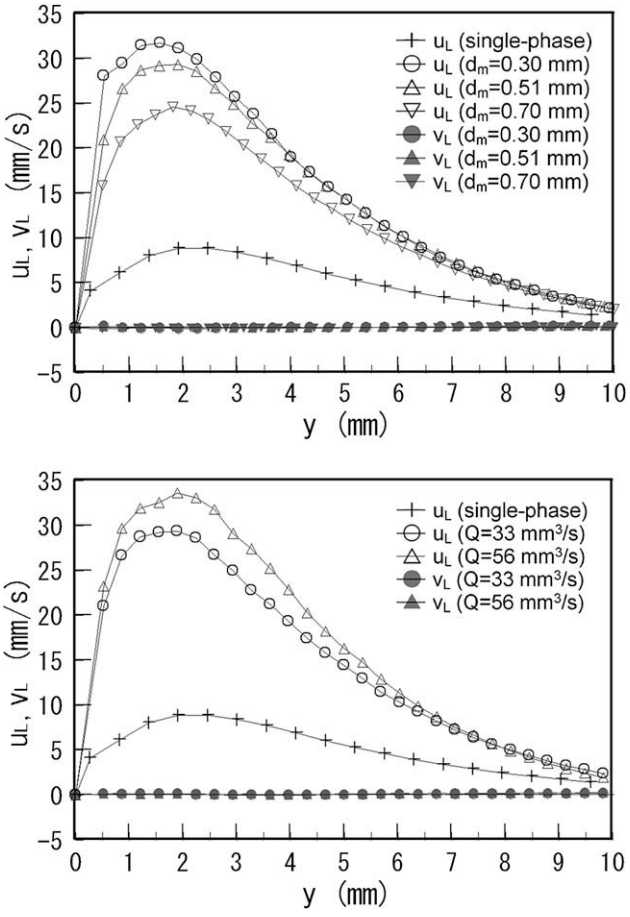

Fig. 15. Profiles of liquid mean velocity.

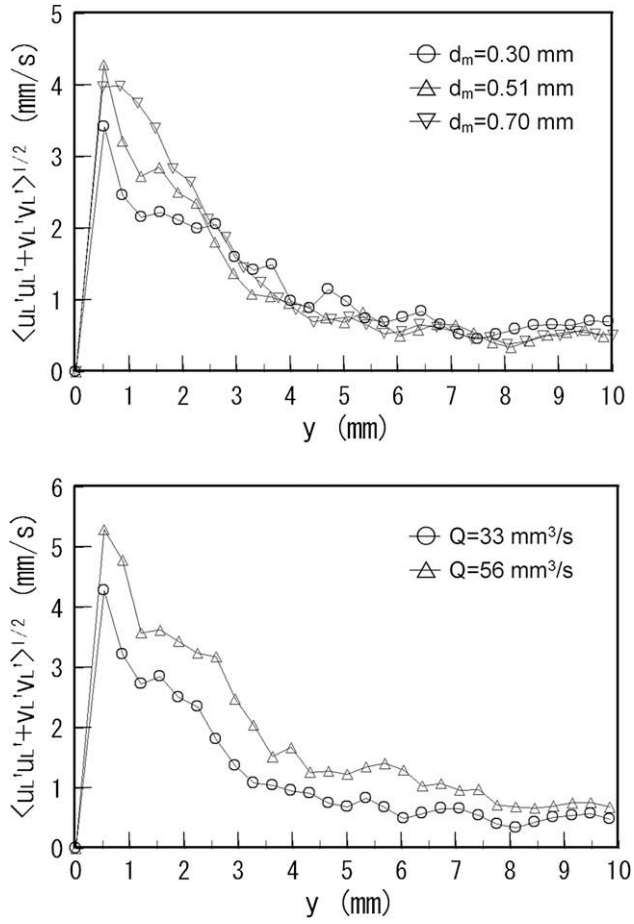

Fig. 16. Profiles of liquid velocity fluctuation.

($Q = 33$ mm^3/s) while case (b) is the result for a constant bubble mean diameter ($d_m = 0.51$ mm). The following points are discussed for these figures:

(1) Both the liquid rise mean velocities and the liquid velocity fluctuations with sub-millimeter-bubble injection are much higher than those without injection. The former leads to advection in the warm liquid while the latter enhances the mixing of warm and cool liquids around the heated plate. Consequently, both enhance heat transfer directly. In this study, the former and the latter are called the "advection effect" and "mixing effect" due to bubbles, respectively.

(2) The liquid rise velocity increases with a decrease in the bubble diameter (see Fig. 15, case (a)). In particular, the increase in the liquid rise velocity for the bubble size reduction is significant near the heated plate. This increase near the heated plate is due to two factors. One is the bubble number density. The bubble number density increases with a decrease in the bubble diameter because case (a) is the result under constant bubble flow rate. Therefore, in the case of smaller bubbles, bubble-induced liquid entrainment, which leads to an increase in the liquid rise velocity near the heated plate, always occurs. The other is the location of bubbles near the heated plate. As shown in Fig. 13, smaller bubbles tend to concentrate near the heated plate. This bubble concentration causes a significant increase in the liquid rise velocity in the vicinity of the heated plate.

(3) The liquid velocity fluctuation increases with the mean bubble diameter (see Fig. 16, case (a)). As is mentioned in Section 6.6, the bubble Reynolds number for $d_m = 0.70$ mm is 2.5–4 times higher than that for $d_m = 0.30$ mm. Bubble-induced velocity fluctuations (e.g., velocity fluctuations induced by displacement of the surrounding liquid around a rising bubble and the wake around a rising bubble) increase with the bubble Reynolds number (Kitagawa et al., 2001), and therefore the liquid velocity fluctuation for $d_m = 0.70$ mm becomes higher.

(4) The liquid rise velocity increases with an increase in the bubble flow rate (see Fig. 15, case (b)). This is mainly due to an increase in the bubble number density. This is because the probability distribution of the bubble diameter is almost independent of the bubble flow rate, which is shown in Fig. 4, and the dependency of the bubble location on the bubble flow rate is weak, according to our analysis. Similarly, the liquid velocity fluctuation increases with the bubble flow rate (see Fig. 16, case (b)). It is concluded from these results that the increase in the bubble flow rate leads to increases in both the advection and mixing effects due to bubbles. The same tendencies were reported in our previous paper (Kitagawa et al., 2008).

6.8. Fractional contribution of each effect due to bubbles to heat transfer enhancement or deterioration

In this section, we estimate the fractional contributions of the effects due to bubbles (i.e., advection, mixing and heat insulation effects) to the heat transfer enhancement or deterioration, based on numerical simulations of natural convection in which the bubble-induced upward flow near the heated plate is considered. Here, the bubble-induced upward flow is essentially different from the flow induced by a wall jet. This is because the former is hardly reduced by the strong viscous effect near the heated wall and continues from the bottom to the top of the container because of bubble buoyancy. Therefore, in our simulations, an ideal driving force F_A is added to the conservation equation of the liquid momentum to accurately express the bubble-induced upward flow near the heated plate.

$$\frac{\partial \mathbf{u}_L}{\partial t} + (\mathbf{u}_L \cdot \nabla)\mathbf{u}_L = -\frac{1}{\rho_L}\nabla p_L + \nu_L \nabla^2 \mathbf{u}_L + (\beta_L(T_L - T_{L,\infty})g + F_A - g)\mathbf{i}_x. \tag{11}$$

From the probability distribution of bubble location shown in Fig. 13, F_A is considered to change in the y direction. In addition, bubbles are located in the region of $y = 0$–2.0 mm, so that F_A in the y direction is given in this region. For these reasons, F_A is defined as

$$F_A = F_{A0} \sin\left(\frac{\pi y}{4\Delta y}\right) (0 \le y \le 4\Delta y), \tag{12}$$

where F_{A0} is the amplitude of the function and ranges from 0.018 to 0.036 N/kg. F_A in the x direction is given from the bottom to the top of the container; i.e., $x = -50$–980 mm. F_A is discretely given at a center of each computation cell.

Each effect due to bubbles is defined by Eq. (13) and illustrated in Fig. 17.

$$FC_A = h_{xA} - h_{x0}, \quad FC_M - FC_H = h_x - h_{xA}, \tag{13}$$

where, FC_A, FC_M and FC_H are the advection, mixing and heat insulation effects due to bubbles, respectively. h_{xA} is the heat transfer coefficient obtained from numerical simulations of natural convection with F_A. In Fig. 17, when $FC_M - FC_H$ is positive, the mixing effect is higher than the heat insulation effect. On the other hand, when $FC_M - FC_H$ is negative, the latter is higher than the former. As described in Section 6.5, in all the cases except for the case of $d_m = 0.30$ mm and $Q = 33$ mm^3/s, the heat insulation effect is considered negligible, so that FC_H is set as zero.

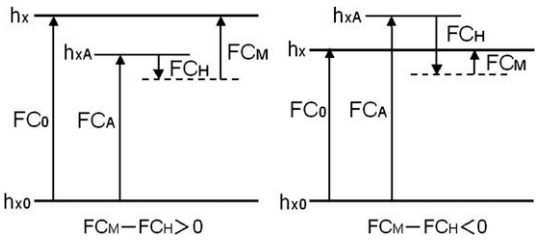

Fig. 17. Outline of each effect due to bubbles.

Fig. 18 shows the profiles of the liquid rise velocity obtained from the numerical simulations. The curves in this figure are obtained by applying the least-square method to the simulation results. The "NC flow" stands for the natural convection flow without F_A. In the region of $y = 0$–10 mm, the liquid rise velocity is increased by the addition of the ideal driving force and increases with F_{A0}. Furthermore, the locations of the peaks in the profiles are around $y = 1.5$ mm. These tendencies are almost same as those shown in Fig. 15 though there are small shifts in the locations of the peaks. Therefore, the addition of the driving force to the conservation equation of the liquid momentum enables us to express the bubble-induced upward flow near the heated plate.

Fig. 19 shows the relationship between $u_{L,max}/y_p$ and h_{xA}. Here, $u_{L,max}$ and y_p are the maximum liquid rise velocity and the y location of a peak in the profile of the liquid rise velocity, respectively. In the present computational conditions, the heat transfer coefficient increases linearly with $u_{L,max}/y_p$. Therefore, using both $u_{L,max}$ and y_p obtained from Fig. 15, h_{xA} is estimated by interpolating the simulated data in Fig. 19 (as indicated by the arrows).

Table 2 gives the heat transfer coefficients and each effect due to bubbles obtained from experimental data and simulation results. In the table, FC_0 ($=h_x - h_{x0}$) is the net increase in the heat transfer coefficient due to the sub-millimeter-bubble injection. Note that FC_M for the case of $Q = 33$ mm^3/s and $d_m = 0.30$ mm is estimated using the relation, which is obtained from liquid velocity fluctuations averaged over the range of $y = 0$–2 mm and FC_M for the other cases. Fig. 20 shows the fractional contribution of the advection and mixing effects due to bubbles to heat transfer enhancement. The following points are discussed for Table 2 and Fig. 20.

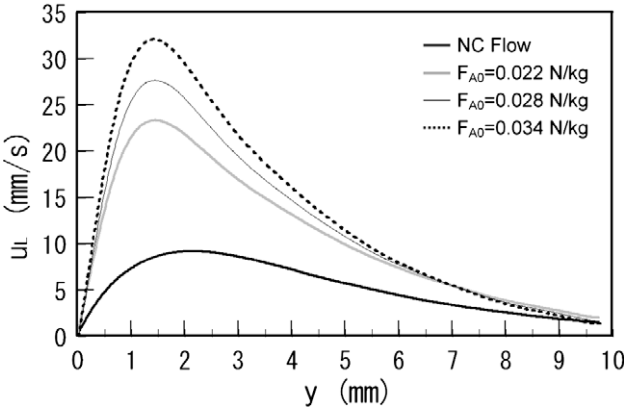

Fig. 18. Profiles of liquid rise velocity obtained from numerical simulations.

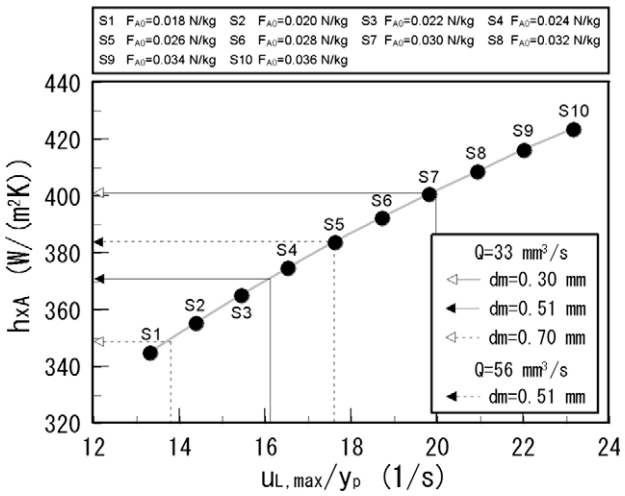

Fig. 19. Relationship between $u_{L,max}/y_p$ and h_{xA}.

Table 2
Heat transfer coefficients and each effect due to bubbles.

Q (mm^3/s)		33		56
d_m (mm)	0.30	0.51	0.70	0.51
$u_{L,max}/y_p$ (1/s)	19.9	16.1	13.8	17.6
h_{xA} (W/m^2 K)	401	371	349	384
h_x (W/m^2 K)	392	382	367	414
h_{x0} (W/m^2 K)	242	242	242	242
$FC_M - FC_H$ (W/m^2 K)	−9	11	18	30
FC_0 (W/m^2 K)	150	140	125	172
FC_A (W/m^2 K)	159	129	107	142
FC_M (W/m^2 K)	6	11	18	30
FC_H (W/m^2 K)	15	0	0	0

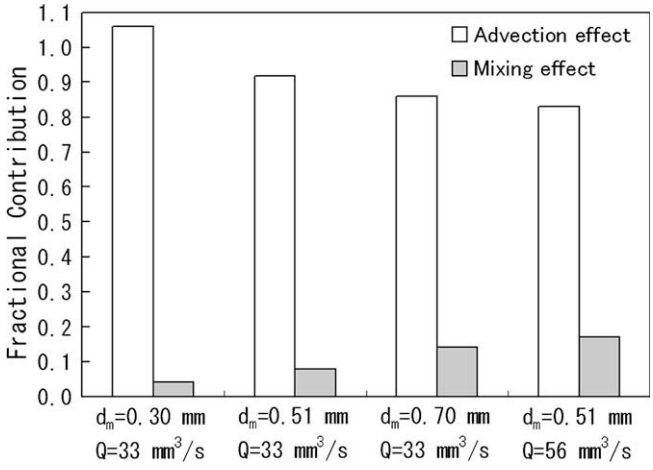

Fig. 20. Fractional contribution of advection and mixing effects due to bubbles to heat transfer enhancement.

(1) For all cases, the contribution of the advection effect to the heat transfer enhancement is large compared with that of the mixing effect and its contribution is higher than 80%. It is therefore considered that the heat transfer enhancement is dominated by the advection effect due to bubbles.
(2) For a constant bubble flow rate (Q = 33 mm^3/s), the fractional contribution of the advection effect increases with a decrease in the mean bubble diameter. In the case of d_m = 0.30 mm, the fractional contribution of the advection effect is higher than 1. However, in this case, the heat insulation effect, which causes heat transfer deterioration, occurs and it corresponds to approximately 10% of the net increase in the heat transfer coefficient. This is due to a decrease in the superficial thermal conductivity associated with the bubble concentration near the heated plate, which is mentioned in Section 6.5. From the above results, we conclude the increase in the heat transfer coefficient ratio for the bubble size reduction, which is shown in Fig. 8, results from an increase in the advection effect due to bubbles. In particular, high heat transfer enhancement for d_m = 0.30 mm is due to a significant advection effect due to bubbles rising close to the heated plate, though there is a heat insulation effect.
(3) For a constant bubble mean diameter (d_m = 0.51 mm), the fractional contribution of the mixing effect increases with the bubble flow rate. This corresponds to the liquid velocity fluctuation increasing with the bubble flow rate (see Fig. 16, case (b)). It is therefore expected that the increase in the heat transfer coefficient ratio for the bubble flow rate, which is shown in Fig. 8, originates from an increase in the mixing effect.

7. Conclusions

The effects of the bubble size on the heat transfer enhancement for the laminar natural convection of water along a vertical heated plate with uniform heat flux were experimentally and numerically investigated. In the temperature and velocity measurements, thermocouples and the PTV technique were used. Moreover, two-dimensional numerical simulations were performed to comprehensively understand the effects of bubble injection on the flow near the heated plate. For mean bubble diameters in the range of 0.30 < d_m < 0.70 mm, the conclusions obtained from measurements and numerical simulations are as follows.

(1) The ratio of the heat transfer coefficient with sub-millimeter-bubble injection to that without injection (i.e., the heat transfer coefficient ratio) ranges from 1.3 to 2.2 and the heat transfer gain reaches approximately 9.7 due to the sub-millimeter-bubble injection. These results clearly demonstrate that sub-millimeter-bubble injection is a highly efficient technique for enhancing the heat transfer for the laminar natural convection of water.
(2) Under the experimental conditions for velocity measurements, the contribution of the advection effect to the heat transfer enhancement is large compared with that of the mixing effect and its contribution is higher than 80%. It is therefore considered that the heat transfer enhancement is mainly dominated by the advection effect due to bubbles.
(3) For a constant bubble flow rate, the heat transfer coefficient ratio increases with a decrease in the mean bubble diameter. It is therefore possible to enhance effectively the natural convection heat transfer by bubble size reduction. Such an increase in the heat transfer coefficient ratio results from an increase in the advection effect due to bubbles. In particular, high heat transfer enhancement for d_m = 0.30 mm is due to a significant advection effect due to bubbles rising close to the heated plate, though the heat insulation effect, which causes heat transfer deterioration, occurs.
(4) For a constant bubble mean diameter, the heat transfer coefficient ratio increases with the bubble flow rate. This increase originates from an increase in the mixing effect.

References

Inagaki, T., Komori, K., 1995. Heat transfer and fluid flow of natural convection along a vertical flat plate in the transition region: experimental analysis of the wall temperature field. Int. J. Heat Mass Transfer 38, 3485–3495.

Kitagawa, A., Murai, Y., Yamamoto, F., 2001. Two-way coupling of Eulerian–Lagrangian model for dispersed multiphase flows using filtering functions. Int. J. Multiphase Flow 27, 2129–2153.

Kitagawa, A., Hishida, K., Kodama, Y., 2005. Flow structure of microbubble-laden turbulent channel flow measured by PIV combined with the shadow image technique. Exp. Fluid 38, 466–475.

Kitagawa, A., Hagiwara, Y., Kouda, T., 2007. PTV investigation of phase interaction in dispersed liquid–liquid two-phase turbulent swirling flow. Exp. Fluid 42, 871–880.

Kitagawa, A., Kosuge, K., Uchida, K., Hagiwara, Y., 2008. Heat transfer enhancement for laminar natural convection along a vertical plate due to sub-millimeter-bubble injection. Exp. Fluid 45, 473–484.

Lloyd, J.R., Sparrow, E.M., Eckert, E.R.G., 1972. Laminar, transition and turbulent natural convection adjacent to inclined and vertical surfaces. Int. J. Heat Mass Transfer 15, 457–473.

Shaukatullah, H., Gebhart, B., 1978. An experimental investigation of natural convection flow on an inclined surface. Int. J. Heat Mass Transfer 21, 1481–1490.

Takewaki, H., Yabe, T., 1987. The cubic-interpolated pseudo particle (CIP) method: application to nonlinear and multi-dimensional hyperbolic equations. J. Comp. Phys. 70, 355–362.

Tamari, M., Nishikawa, K., 1976. The stirring effect of bubbles upon the heat transfer to liquids. Jpn. Res. Heat Transfer 5, 31–44.

Tokuhiro, A.T., Lykoudis, P.S., 1994a. Natural convection heat transfer from a vertical plate-I. Enhancement with gas injection. Int. J. Heat Mass Transfer 37, 997–1003.

Tokuhiro, A.T., Lykoudis, P.S., 1994b. Natural convection heat transfer from a vertical plate-II. With gas injection and transverse magnetic field. Int. J. Heat Mass Transfer 37, 1005–1012.

Vliet, G.C., 1969. Natural convection local heat transfer on constant-heat-flux inclined surfaces. ASME. J. Heat Transfer 91, 511–516.

Vliet, G.C., Liu, C.K., 1969. An experimental study of turbulent natural convection boundary layers. Trans. ASME J. Heat Transfer 91, 517–531.